A Modified Inverse Vector Hysteresis Model for Nonoriented Electrical Steels Considering Anisotropy for FEA

Shuaichao Yue, Philip I. Anderson, Yongjian Li, Qingxin Yang and Anthony J. Moses

Abstract- **This paper presents a modified Mayergoyz-based vector hysteresis model to describe the anisotropic material behavior of nonoriented (NO) steels over a wide range of rotational excitations. The proposed model adopts a new representation of a vector Everett function, which is actually an elliptical interpolation motivated by the real anisotropic behavior of NO steel, to deal with the uniaxial anisotropy characteristic, which is especially pronounced at low induction levels. The biaxial anisotropy occurring at high densities is described by a nonlinear coefficient, which is actually a function of the magnitude of magnetic flux density. A systematic identification algorithm is given in detail. The validity of this model is verified through comparison with experimental data under both alternating and rotational excitations. The 2-D finite element analysis (FEA) of incorporating this model into TEAM problem 32 simulation is also illustrated.**

Index Terms— **Macroscopic magnetic anisotropy, vector hysteresis model, nonoriented electrical steels.**

I. Introduction

ELECTRICAL steels are widely utilized in the cores of electrical equipment. On one hand, it has long been known that rotating magnetic flux widely exists in certain parts of magnetic cores such as the T-joints of multiphase transformers and behind the teeth of rotating machines. Extensive reports [1-3] also show that the resulting rotational core loss contributes greatly to the total core loss. On the other hand, for most commercial FEA software, the intrinsic hysteresis relationship between magnetic flux density B and magnetic field strength H is usually approximated by a linear or single-valued magnetization curve [4] which leads to the inaccuracy in magnetic field distribution prediction and core loss calculation. Therefore, it is essential that the vector magnetic properties of electrical steels are properly modeled and applied to FEA in order to improve the precision of electromagnetic numerical calculations.

Many kinds of hysteresis models have been proposed based on the physical or analytical descriptions of the material hysteresis behavior. For example, the Jiles-Antherton (JA) model is derived from the energy equilibrium during domain-wall motion [5]. This model uses five equations to describe the hysteresis phenomenon. The Preisach model, consisting of a set of unidirectional relay operators, is phenomenological and widely used for its high accuracy and simplicity [6]. In addition, Stoner and Wohlfarth (SW) proposed a vector model by introducing a single domain operator with uniaxial anisotropy [7] .This is a vector model and is very useful for investigating

the magnetization process but it does not produce accurate hysteresis loops. The interactions of magnetic domains are also neglected in this model. In order to describe vector hysteresis better, Mayergoyz developed a vectorization method based on superposition of the scalar Preisach model along all possible directions [8]. This is a general method and theoretically, can be applied to any scalar model to enhance it to a vector approach.

The Mayergoyz-based models have attracted attention of many researchers because of its applicability and expansibility. The original Mayergoyz model is ideally isotropic which means with a circular H input, we can obtain a circular B and vice versa [9]. This is obviously not consistent with the results of rotational excitation experiment for anisotropic NO steel. Therefore, an extended version which introduced an exponential term w into the projected component of the input was proposed by Adly and Mayergoyz (Adly-Mayergoyz Model) to reproduce the observed saddle-like shape of the magnetic field strength trajectory at high excitation [10]. Based on this model, Dlala et al. presented another improved model by using an additional phase shift parameter to further improve the prediction precision of core loss at high excitations (Improved Model) [11]. However, a common limitation of the above two models is that they neglect the dominating uniaxial anisotropy at low induction since the isotropic distribution function (or Everett function) is adopted for all directions, as discrepancies with experimental data are observed. Zhu et al. proposed another vector hysteresis model which tried to characterize the anisotropy over a wide excitation range by using a new parameter dependent on the magnitude and direction of the magnetic field [12]. However, this method requires a large amount of experimental data for identification. In addition, other vector models which take into account the anisotropy, for instance, the Preisach-type vector moving model [13] and the SW-type model with single hysteresis operator [14], have been proposed recently. These models are proved to have high accuracy, at the expense of requiring complete measured data. A detailed review of vector hysteresis models and corresponding identification methods is given in [15].

The incorporation of a hysteresis model into FEA must deal with several problems. Firstly, most hysteresis models (forward model) traditionally use H as input and B (or magnetization M) as output. However, the FEA problem is usually formulated by magnetic vector potential, which makes B the output of differential equations. As a result, an additional iteration process for solving H has to be applied when the forward model is used [16]. Secondly, when anisotropy is taken into account,

vector hysteresis models are more reasonable than scalar ones [17, 18] since the calculated magnetic field quantities from FEA are essentially vectors. Thirdly, although the Newton-Raphson method has been successfully applied to solving nonlinear FEA problems with its rapid convergence near the solution, it cannot always ensure convergence especially when hysteresis is involved. In this case, the differential permeability may be discontinuous. Under this condition, the more robust fixed-point iteration technique is usually preferred for its stable convergence [19].

In this paper, a description of Mayergoyz-based vector hysteresis models along with macroscopic anisotropy analysis of NO steel is given. Then, a modified inverse vector hysteresis model is proposed to accommodate the anisotropic behavior over a wide magnetic flux density range. The inverse form of this model simplifies its coupling with FEA. The novelty of this model lies in its combination of a new representation of the Everett function and a nonlinear coefficient. The new Everett function is based on the real anisotropic behavior of NO steel in order to better reproduce elliptical vector $\boldsymbol{H}$ loci at low excitation levels. The nonlinear coefficient is used for characterizing the anisotropy, especially at high inductions. A systematic identification procedure is explained in detail. By comparing with experimental results of 0.35mm thick NO steel under both alternating and rotational excitations, the effectiveness of this proposed model is validated. The application of incorporating this model into FEA of TEAM problem 32 [31], which is a benchmark designated to test vector hysteresis models, by the fixed-point iteration technique and a time-stepping scheme is also demonstrated. In addition, the proposed model is useful for the magnetic field analysis of other electromagnetic devices such as electrical machines considering both hysteresis and anisotropy properties.

II. Mayergoyz-based Vector Hysteresis Model

A. Evolution of the Mayergoyz-based Model

The Preisach-Type vector hysteresis model was first proposed by Mayergoyz [9]. The magnetic field strength $\boldsymbol{H}$ is expressed as the superposition of a continuously distributed scalar model along $\boldsymbol{e}_\varphi$ direction in the rolling plane.

$$\boldsymbol{B}(t) = \int_{-\pi/2}^{\pi/2} \left(\iint_{\alpha \geq \beta} \mu(\alpha,\beta)\gamma[H_\varphi(t)]d\alpha d\beta \right) \boldsymbol{e}_\varphi d\varphi \quad (1)$$

where $\gamma[H_\varphi]$ is the relay operator that is controlled by the increasing value α and the decreasing value β of H_φ. To avoid the double integral, the Preisach distribution function $\mu(\alpha,\beta)$ can be replaced by Everett function. H_φ is the projection of input in the direction φ and can be calculated as

$$H_\varphi = |\boldsymbol{H}|\cos(\theta_H - \varphi) \quad (2)$$

where θ_H is the polar angle of magnetic field strength $\boldsymbol{H}$.

The above Mayergoyz model is isotropic. In order to accommodate the real vector magnetic field trajectory known from experiment, Adly and Mayergoyz [10] presented an extended version of this model by modifying the projection term as

$$H_\varphi = |\boldsymbol{H}|\,\delta\,\left|\cos(\theta_H - \varphi)\right|^{1/w} \quad (3)$$

where $\delta = \text{sign}[(\theta_H - \varphi)]$. The use of $w > 1$ creates the effect of anisotropy at high induction in this model and thus the loci of magnetic field strength show saddle-like shape. Note that the Adly-Mayergoyz model becomes the original Mayergoyz model when $w=1$.

Another extension is given by Dlala et al. to improve the core loss character near to saturation [11]. An additional small phase shift parameter ψ is introduced.

$$H_\varphi = |\boldsymbol{H}|\,\delta\,\left|\cos(\theta_H - \varphi + \psi)\right|^{1/w} \quad (4)$$

where ψ is associated with rotational core loss and can be experimentally identified.

B. Macroscopic Anisotropy Analysis of NO Steel

Theoretically, an isotropic magnetic material is supposed to exhibit the same properties in all directions due to the assumed random orientation of all its grains. In fact, it's difficult to produce ideally isotropic material because the manufacturing processes usually introduce anisotropy. For example, rolling processes will inevitably elongate grains along the rolling direction (RD, y-axis), resulting in a uniaxial anisotropy along the RD. Here, we focus on the macroscopic anisotropy of NO steel displayed from experiment. According to extensive experimental results[20-23], NO steel exhibits complicated anisotropic behavior dependent on magnetic flux density level and frequency. Since the scope of this paper is rate-independent field, we only discuss the trajectory of $\boldsymbol{H}$ under circular $\boldsymbol{B}$ at quasi-static frequency, which gives information about the macroscopic anisotropy. As shown in Fig. 1, the $\boldsymbol{H}$ loci appear as ellipses whose major axes (i.e., hard axes) are approximately along the transverse direction (TD, x-axis) in the low flux density range, which implies that uniaxial anisotropy dominates. As $\boldsymbol{B}$ increases, the uniaxial anisotropy seems to gradually decrease, and the four corners of the $\boldsymbol{H}$ loci emerge, which makes them first circular and eventually a saddle-like shape. Here we call this phenomenon the enhancing biaxial anisotropy. Note that in this paper, the boundary between high and low inductions is approximately 1 T. We choose this value because biaxial anisotropy begins to appear in the $\boldsymbol{H}$ loci at higher values. It should be stressed that the distinction between the RD and TD still exists at high inductions, thus it is always easier to magnetize along the RD than along the TD.
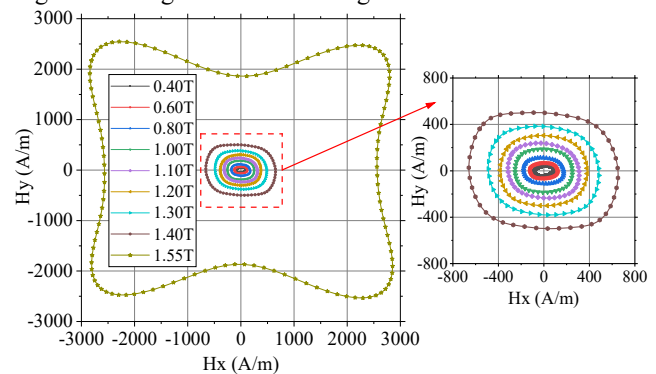
Fig. 1. Loci of measured vector $\boldsymbol{H}$ under circular excitations with amplitudes from 0.4 T to 1.55 T at 5 Hz.

C. Proposed Modified Inverse Vector Hysteresis Model

When modelling NO steel, the macroscopic anisotropic behavior gradually changes from uniaxial anisotropy (ellipse-like **H** loci) to biaxial (saddle-like **H** loci) with increasing magnetic field. All of the improved models (3)-(4) are still ideally isotropic (when $w=1$) because they adopt an identical distribution function (or Everett function) in all directions, which means a circular input generates a circular output. The introduction of $w>1$ results in saddle-like **H** loci only for high inductions, while the model output at low induction remains approximately circular which does not agree with the experimental results. Therefore, a modified vector model which employs a new representation of the Everett function is given to characterize the uniaxial anisotropy of NO steel, which is especially pronounced for low flux densities. Expressing w as a function of magnetic flux density amplitude B_p enables better matching with the experimental data since the biaxial anisotropic behavior of NO steel gradually enhances with increasing excitations as discussed. This model is directly inverted by exchanging the role of **B** and **H** in (1). The computer realization of this model can be approximated as

$$H(t) = \sum_{i=1}^{N} e_{\varphi i} H_{\varphi i}[B_{\varphi i}]\Delta\varphi \qquad (5)$$

where $\varphi i=-\pi/2+(i-1)\pi/N$, $(\Delta\varphi=\pi/N)$ and $i=1,2\ldots N$. N is the number of directions. N affects the calculation accuracy and calculation time, especially when applied to FEA. In this paper, $N=30$ is used to ensure relatively fast and accurate calculation.

The input projection of magnetic flux density along direction φi is given as

$$B_{\varphi i} = |\boldsymbol{B}|\delta \left|\cos(\theta_B - \varphi i + \psi(|B_p|))\right|^{1/w(|B_p|)} \qquad (6)$$

where $w(|B_p|)>1$ and controls the appearance of biaxial anisotropy at high induction. It can be deduced from the above discussion that $w(|B_p|)$ should approach unity with decreasing **B** and increase with increasing **B**. Here, a generalized form that contains three positive coefficients to be identified is given as

$$w(|B_p|) = a + b|B_p|^c \qquad (7)$$

As pointed out in [11], the value of ψ has no significance for the hysteretic region while it does have an influence at the near saturation region since at this stage the phase lag between **B** and **H** is already very small. For circular excitation, ψ is expressed as

$$\psi(|B_p|)=e^{(-d|B_p|+e)}|B_p| \qquad (8)$$

When using the vector Everett function $E(\alpha,\beta)$ instead of the distribution function, for a given direction φi, the scalar inverse hysteresis model calculates $H_{\varphi i}$ when $B_{\varphi i}$ is increasing $(dB_{\varphi i}/dt>0)$ as

$$H_{\varphi i}(t)=2\sum_{k=1}^{Q}\left[E_{\varphi i}(\alpha_k,\beta_{k-1})-E_{\varphi i}(\alpha_k,\beta_k)\right]+2E_{\varphi i}(B_{\varphi i}(t),\beta_Q) \qquad (9)$$

And when $B_{\varphi i}$ is decreasing $(dB_{\varphi i}/dt<0)$ as

$$H_{\varphi i}(t)=2\sum_{k=1}^{Q}\left[E_{\varphi i}(\alpha_k,\beta_{k-1})-E_{\varphi i}(\alpha_k,\beta_k)\right] \qquad (10)$$

where α_k and β_k are the increasing and decreasing sequences of $B_{\varphi i}$ stored by staircase line. $k=1, 2,\ldots Q$ correspond to the reversal points representing magnetization history.

Theoretically, an accurate vector model requires the Everett function along all directions. However, it is not realistic to measure the magnetic properties along every direction. Thus, considering the real anisotropic behavior of NO steel as analyzed previously, an elliptical interpolation function continuously transforming from the RD to TD is used to approximate the vector Everett function at a given direction φi

$$E_{\varphi i}(\alpha,\beta) = \sqrt{\frac{E_{RD}(\alpha,\beta)^2 E_{TD}(\alpha,\beta)^2}{E_{RD}(\alpha,\beta)^2 \sin^2\varphi i + E_{TD}(\alpha,\beta)^2 \cos^2\varphi i}} \qquad (11)$$

where $E_{RD}(\alpha,\beta)$ and $E_{TD}(\alpha,\beta)$ are the vector Everett function along the RD and TD respectively. In this way, an elliptical vector Everett function is generated and can be used in the calculation. Fig. 2 demonstrates the output of this modified vector Everett function along different directions.
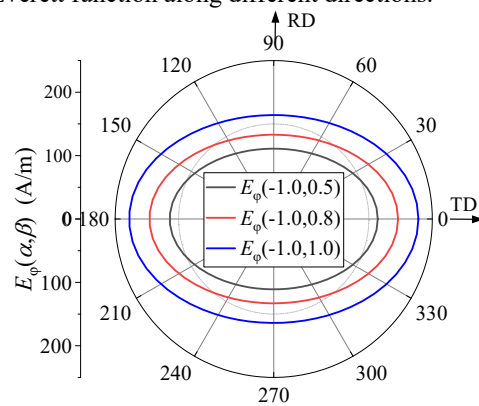
Fig. 2. Output of the modified vector Everett function along different directions.

Fig. 3 shows the output of the modified inverse vector model with an ideally circular **B** input. The improved Mayergoyz model (4) is used for comparison since it is believed to be more accurate than the other two versions. It can be seen that, compared with the improved model, a difference is introduced between the RD and TD to compensate for the intrinsic uniaxial anisotropy of NO steel along the RD by using the new representation of the Everett function.
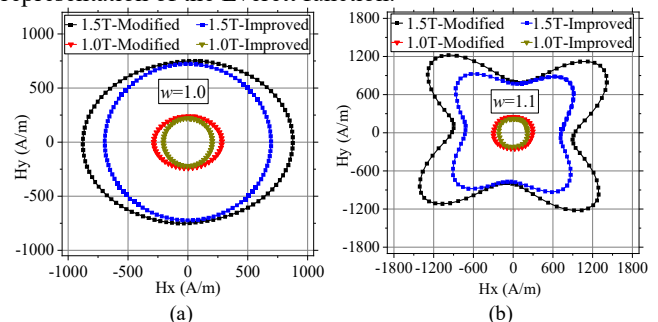
Fig. 3. Output comparison of modified and improved models under ideally circular excitation with different w values. (a) $w=1$. (b) $w=1.1$.

III. PARAMETER IDENTIFICATION PROCEDURE

The identification of this modified inverse vector hysteresis model (5-11) involves the estimation of $E_{RD}(\alpha,\beta)$, $E_{TD}(\alpha,\beta)$, w and ψ. Firstly, by constructing the first-order reversal curves (FORCs) from the measured alternating major hysteresis loops at quasi-static frequency (5 Hz), the scalar Everett functions along the RD and TD can be approximated. Next, the

corresponding vector Everett functions can be obtained by the transition formulations between the vector and scalar Everett function. Secondly, the value of w is determined from the rotational experimental data at three induction levels (0.4 T, 0.8 T and 1.55 T). By using an algorithm based on the Nelder-Mead Simplex Method [24], w is optimized such that the error between the model output and the measured vector loci of magnetic field strength is minimized. After determining the vector Everett function and w, the small phase shift ψ can be obtained by comparing the calculated and measured rotational loss data.

A. First-order Reversal Curves

Direct measurement of the FORCs is difficult and usually requires a large amount of experimental data. Thus, some analytical expressions are derived based on different distribution functions [25, 26]. In addition, Naidu [27] proposed another simple method (12-13) that uses the descending branch of the major hysteresis loop $B_m(H)$ to model hysteresis and this is applied to the approximate FORCs by Dlala [28].

$$B(H) = 2F(-H)F(H) - B_{\mathrm{m}}(-H) \qquad (12)$$

where

$$F(H) = \begin{cases} \sqrt{|B_{\mathrm{m}}(H)|} & H \le 0 \\ \dfrac{B_{\mathrm{m}}(H) + B_{\mathrm{m}}(-H)}{2\sqrt{B_{\mathrm{m}}(H)}} & H > 0 \end{cases} \qquad (13)$$

The descending branch from experiment is used to create a 1-D linear interpolation operator $\Phi(x; H; B)$ to describe the relationship between H and B, where x is an independent variable and H, B represent the data used for interpolation. This is performed by equally partitioning the magnetic field strength in the range $[-H_{\mathrm{m}}, H_{\mathrm{m}}]$ into n points, and the corresponding B values are $B_{\mathrm{m}} = [B_{\mathrm{m1}}, B_{\mathrm{m2}}, \ldots, B_{\mathrm{mn}}]$.

Since this Everett function uses B as an input (independent variable), α is uniformly divided in the interval $[-B_{\mathrm{m}}, B_{\mathrm{m}}]$ by m points, where $\alpha_1 > \alpha_2 > \ldots > \alpha_m$. The descending curve can be rewritten by the interpolation operator as

$$H_{\mathrm{mj}} = \Phi(\alpha_j; [H_1, H_2, ..H_n]; [B_{m1}, B_{m2}, ..B_{mn}]), \quad j = 1, 2, ... m \quad (14)$$

Then, based on Dlala's work, the FORCs can be approximated by the following equations

$$H_{\mathrm{rij}} = \frac{i-1}{m-1}(H_m - H_{mj}) + H_{mj} \qquad (15)$$
$$B_{rij} = 2F(-H_{mj})F(H_{rij}) - B_m(H_{rij})$$

where $i=1, 2, .., n$ and $j=1, 2, \ldots, m$. Up until this step, the FORCs are initially established. Each column of matrices H_{rij} and B_{rij} correspond to one FORC. The linear operator is then used for each column to produce the FORC controlled by a uniform B step (16). Fig. 4 shows the measured major hysteresis loops for constructing FORCs and it can be seen that there is a slight difference between the RD and TD, especially at high induction. Fig. 5 illustrates the constructed FORCs of the RD and TD respectively.

$$H_{\mathrm{forc}ij} = \Phi(\alpha_i; [H_{r1j}, H_{r2j}, ..H_{rnj}]; [B_{r1j}, B_{r2j}, ..B_{rnj}]) \qquad (16)$$
$$\text{for} \quad j = 1, 2, .., m; \qquad i = 1, 2, .., j;$$

Based on the FORCs, the scalar Everett function can be easily calculated from the following equation

$$F(\alpha, \beta) = \frac{1}{2}(H_{\mathrm{forc}}(\alpha, \beta) - H_{\mathrm{forc}}(\alpha)) \qquad (17)$$

where $H_{\mathrm{forc}}(\alpha, \beta)$ refers to the H value corresponding to FORCs, and $H_{\mathrm{forc}}(\alpha)$ to the value of H at the reversal point.
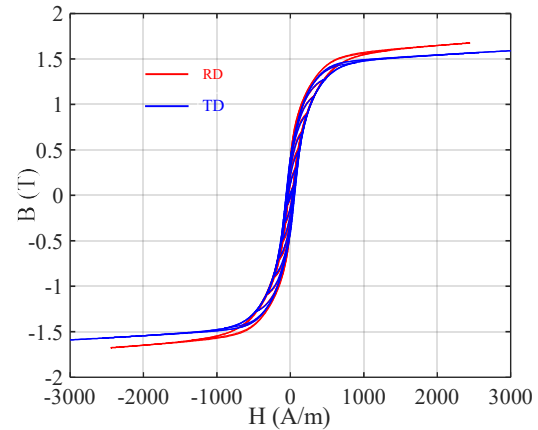
Fig. 4. The measured alternating hysteresis loop along the RD and TD at 5 Hz.
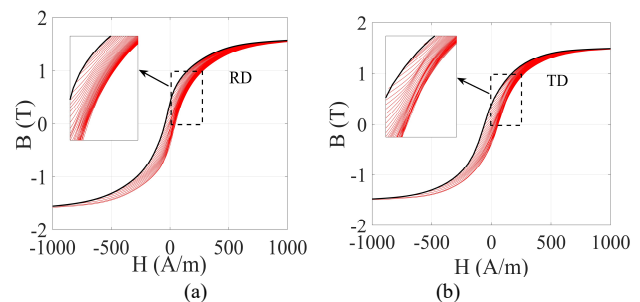
Fig. 5. The descending branch (black) and constructed FORCs (red) along the RD and TD. m=100, n=100. (a) RD. (b) TD.

B. Vector Everett Function

After obtaining the scalar Everett function in the RD and TD, the following well-known formulae (18-19) [29] describing the relationship between the scalar and vector Everett functions (when assuming isotropy) can be used to obtain the corresponding vector functions. A closed form solution is given by Mayergoyz as shown in (19), where $F(\alpha,\beta)$ and $E(\alpha,\beta)$ represent scalar and vector Everett function respectively. By varying λ from 0 to 1, all the required values of $E(\alpha,\beta)$ can be calculated. Fig. 6 illustrates the precalculated vector Everett function over a discretized 100 x 100 mesh region along the RD, 45° from the RD and the TD respectively. Note that the scalar Everett function is not given here since it has a similar shape to the vector function but with different magnitudes.

$$F(\alpha, \beta) = \int_{-\pi/2}^{\pi/2} \cos\varphi \, E(\alpha\cos\varphi, \beta\cos\varphi) \, d\varphi \qquad (18)$$

$$E(\alpha, \lambda\alpha) = \int_0^\alpha \frac{F(s, \lambda s) + s\dfrac{d}{ds}F(s, \lambda s)}{\sqrt{\alpha^2 - s^2}} \, ds \qquad (19)$$

(a)

(b)

(c)
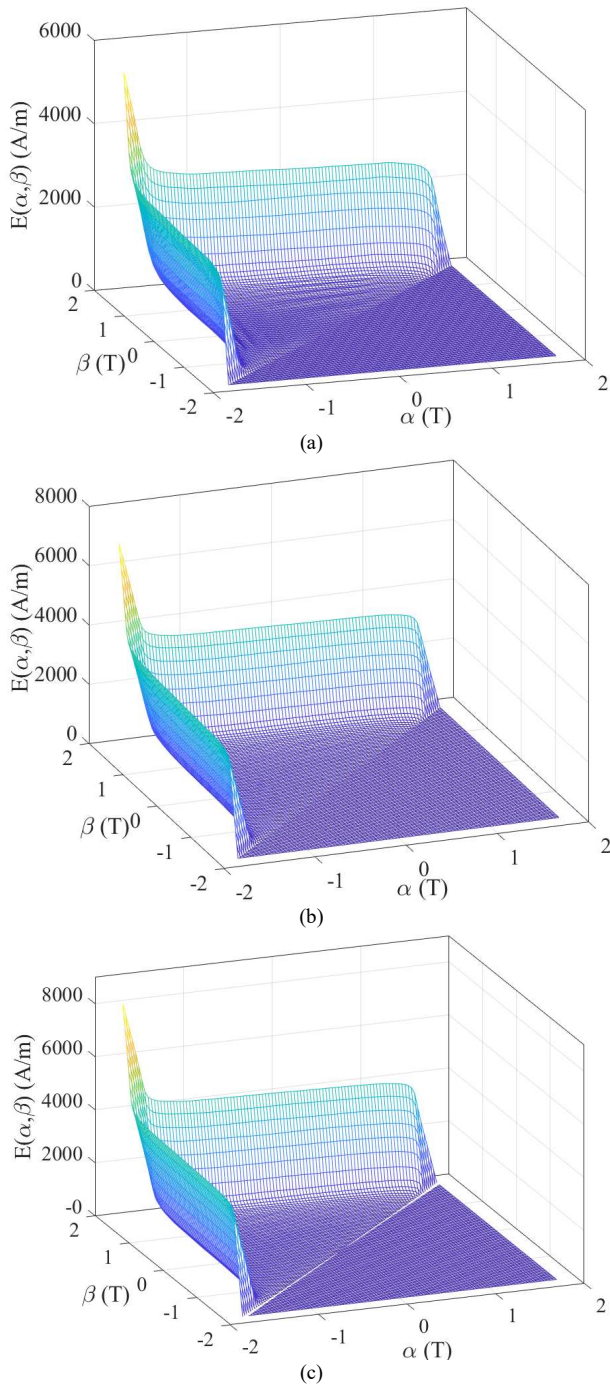
Fig. 6. The calculated vector Everett function along (a) RD. (b) 45° from RD. (c) TD.

C. Bilinear Interpolation for Everett Function

To improve the computation speed, a triangular region with Everett function values stored in vertices of the uniform grids is tabulated, as shown in Fig. 7. For any reversal point (α,β), the corresponding $E(\alpha,\beta)$ can be calculated by bilinear interpolation from this table.
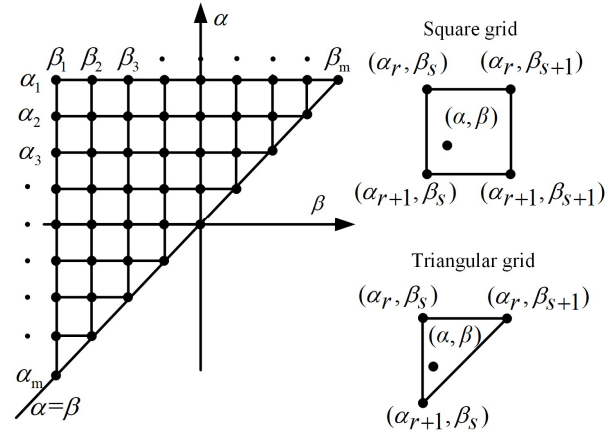
Fig. 7. The uniformly discretised triangular Preisach plane for storing the Everett function values.

For a square grid specified by two position variables r and s, the value of the internal point (α,β) is expressed as

$$E(\alpha,\beta) = C_0 + C_1\alpha + C_2\beta + C_3\alpha\beta \tag{20}$$

where C=[C_0, C_1, C_2, C_3] is the coefficient of this grid and can be calculated as C=A^{-1}b. A^{-1} represents the inverse of matrix A.

$$A = \begin{bmatrix} 1 & r & s & rs \\ 1 & r & s+1 & r(s+1) \\ 1 & r+1 & s & (r+1)s \\ 1 & r+1 & s+1 & (r+1)(s+1) \end{bmatrix} \quad b = \begin{bmatrix} E(\alpha_r,\beta_s) \\ E(\alpha_r,\beta_{s+1}) \\ E(\alpha_{r+1},\beta_s) \\ E(\alpha_{r+1},\beta_{s+1}) \end{bmatrix} \tag{21}$$

For the triangular grid, the vector Everett function value of internal point (α,β) is expressed as

$$E(\alpha,\beta) = C_0 + C_1\alpha + C_2\beta \tag{22}$$

D. Identification Results

Fig. 8 summarizes the necessary steps in the identification procedure. Following these steps, the vector Everett function of the RD and TD is shown in section III, B. Fig. 9 illustrates the parameter w as a function of the magnetic flux density amplitude B_p. An exponential expression of w is given with coefficients a, b, c equal to 1.0270, 0.0438 and 2.5830 respectively. It is also found that in the range 0.40 T-0.80 T, the use of $\psi = 0$ can produce relatively accurate core loss data with an error less than 6.3%. In the range of 1.00 T-1.55 T, the optimal values of ψ are calculated from (8) with d=2.5130 and e=1.8930. The identified parameters for B35A210 are shown in Table I. Note that, the exponential parameter w and phase parameter ψ are responsible for the magnetic field loci and core loss respectively. Small changes in the two parameters will lead to significant changes in vector $\boldsymbol{H}$ loci and core loss values. For example, the increase of w (from 1.0 to 1.1) can substantially change the $\boldsymbol{H}$ loci as shown in Fig. 3. The use of optimal ψ=0.23 (instead of constant 0) at 1.55 T reduces the core loss from 27.7 mJ/kg to 15.6 mJ/kg as shown in Fig. 14.
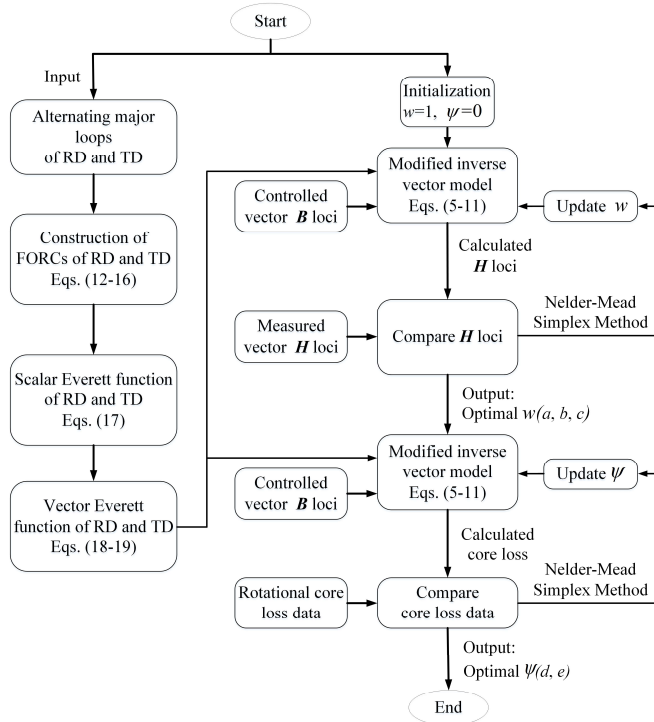
Fig. 8. Flowchart illustrating the parameter identification procedure of the modified model.
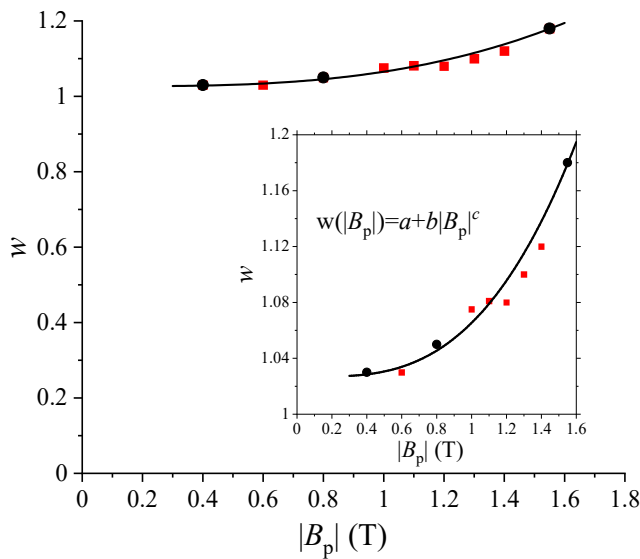
Fig. 9. Coefficient *w* expressed as a function of magnetic flux density amplitude B_p. Three measured vector loci of magnetic field strength are used to determine the parameters *a*, *b* and *c* (black dots). Red squares represent the optimal *w* at other flux levels.

TABLE I
PARAMETERS OF PROPOSED MODEL

Parameter	$w(a,b,c)$			$\psi(d,e)$	
Coefficient	*a*	*b*	*c*	*d*	*e*
Value	1.0270	0.0438	2.5830	2.5130	1.8930

IV. VALIDATION AND RESULTS

A. Testing System

The measurement system consists of a computer equipped with data acquisition card (DAQ), power amplifiers and the double-yoke vertical magnetizer itself as shown in Fig. 10. The orthogonal components of magnetic flux density and magnetic field strength are acquired by needles and tangential coils, which are mounted on a printed circuit board (PCB). The 50 x 50 mm square sample together with the PCB constitutes the ***B-H*** sensing box. The induced voltages are amplified before they are fed to the DAQ. The frequency domain feedback algorithm with a harmonic compensation method proposed by [30] is implemented to control the loci of vector ***B***.
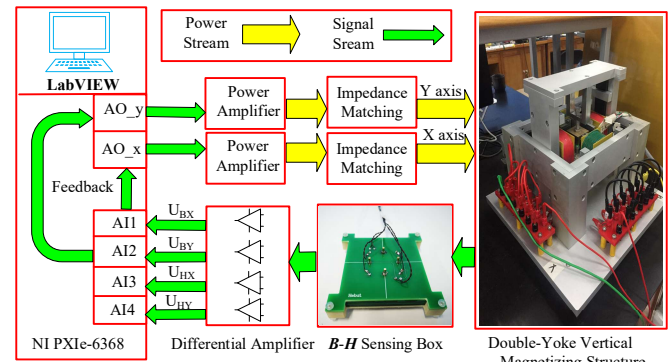
Fig. 10. Rotational magnetic properties measurement system.

B. Magnetic Field Loci

The modified model is applied to the investigation of 0.35 mm thick NO steel B35A210, under both alternating and rotational excitations at 5 Hz. The repeatability of the measurement is verified (above 97%) by repeating the alternating experiment (5Hz) three times. The sample was taken out and returned to the sensing box between each measurement. Comparisons between measured and calculated hysteresis loops with different alternating excitations are given in Fig. 11. There is good agreement between the curves. The overall relative deviation of the ***H*** trajectory is less than 11% and even better at high inductions.
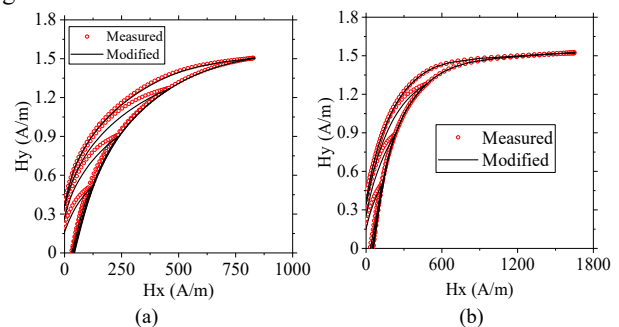
Fig. 11. Comparisons between measured hysteresis loops and those calculated using the modified model along (a) RD (b) TD.

Fig. 12(b) and (d) illustrate the comparison of measured and calculated vector ***H*** loci using the improved model and modified model under circular excitation with B_p=1.55 T, 0.80 T, respectively. The corresponding excitations are shown in Fig. 12(a) and (c). It can be seen the modified model gives a better

fit with the measured data, especially in the TD.

Fig. 13(b) and (d) show the comparison of measured and calculated vector H loci using the modified model under circular excitations, which are shown in Fig. 13 (a) and (c), for the range of 0.4 T-1.4 T. It can be seen that the proposed model can describe the behavior of the H loci accurately over a wide range of rotational magnetic fields. This is mainly achieved by the adoption of the new representation of the vector Everett function and nonlinear coefficient w. In the low induction range, w is relatively small as shown in Fig. 9, and the anisotropy is dominated by the new vector Everett function, thus the H loci appear like ellipses with their major axes along TD. With B increasing, w increases and the anisotropy introduced by w starts to rule, and thus the four corners of H loci emerge, causing H to first be circular and finally saddle shaped. It should be emphasized that because the output of the proposed model is controlled by a combined effect as explained above, it seems there is no apparent correlation between the prediction accuracy of H loci and induction levels.
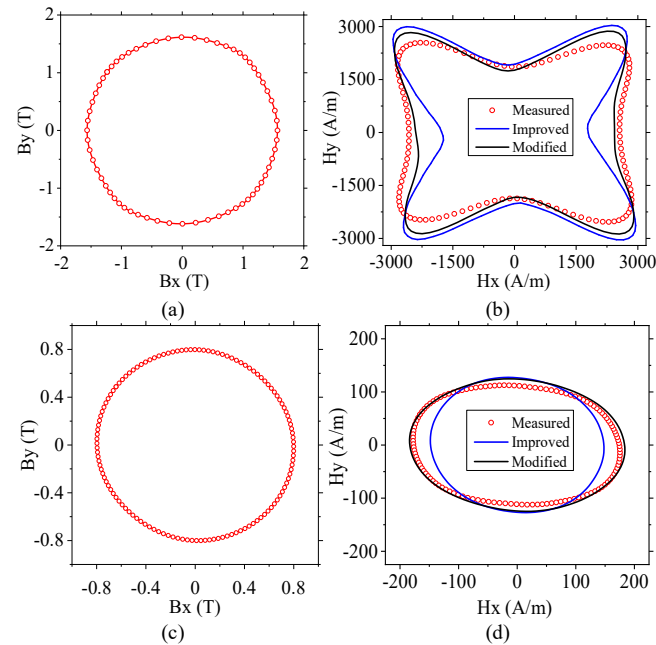
Fig. 12. Comparison of H loci of improved model, modified model and measured data under rotational excitations. (a) Controlled B locus at 1.55 T. (b) Comparison of H loci of 1.55 T. (c) Controlled B locus at 0.80 T. (d) Comparison of H loci of 0.80 T.
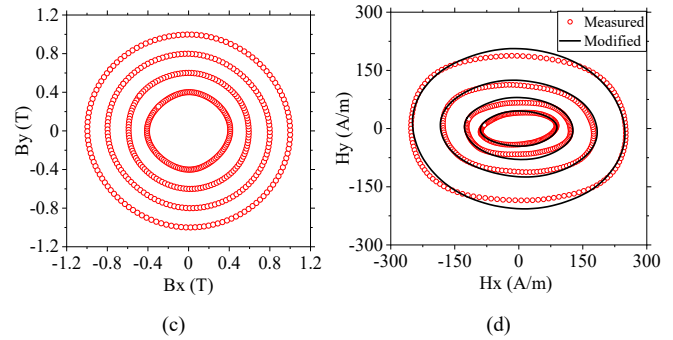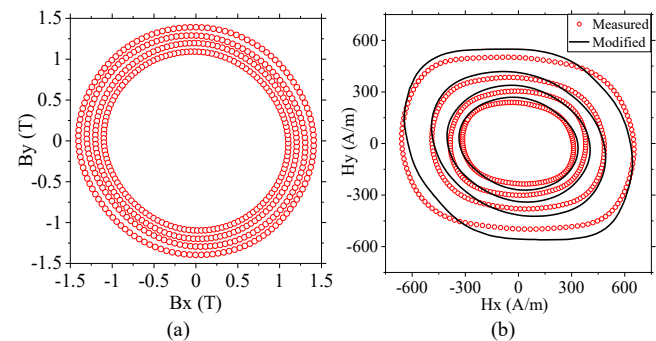
Fig. 13. Comparison of H loci of modified model and measured data under different rotational excitations. (a) Controlled B loci from 1.1 T to 1.4 T. (b) Comparison of H loci for 1.1 T-1.4 T. (c) Controlled B loci from 0.4 T to 1.0 T. (d) Comparison of H loci for 0.4 T-1.0 T.

C. Core Loss Property Discussion

The comparison of rotational core loss calculated with constant value and optimal value is shown in Fig. 14. It should be pointed out that ψ is identified after w has been determined. The red line in Fig. 14 corresponds to the calculated results of Fig. 12 and Fig.13 where a constant phase parameter (ψ=0) is used. Note that in this case although this model can produce relatively accurate H loci over a wide B range, the precision of core loss prediction drops rapidly with increasing B, especially at high inductions. This is actually an intrinsic property of Mayergoyz-based models which use a constant phase parameter (i.e., ψ=0). Due to the core loss being equivalent to the algebraic sum of core losses dissipated in all adopted directions, for each direction φi, the projected magnetic field components $H_{\varphi i} - B_{\varphi i}$ are actually described by a scalar hysteresis model where the corresponding core loss continues to increase with increasing B_{p}. Therefore, the resulting total core loss from the algebraic sum will always increase as B_{p} increases, which is obviously inconsistent with the measured rotational core loss. The use of optimal ψ values bring down the core loss at high inductions by introducing a phase correction between $H_{\varphi i} - B_{\varphi i}$ field components as shown by the blue line in Fig. 14, at the expense of increasing prediction error for the H loci. This shows a limitation of this model that it fails to reproduce the loss property at relatively high inductions. However, it should be emphasized that the primary goal of this model is to improve the precision of H loci approximation, especially in the TD.
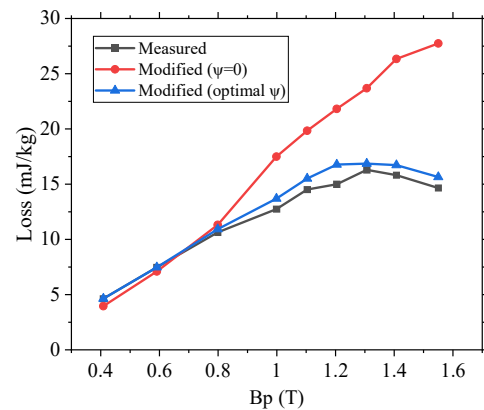
Fig. 14. Comparison of rotational core loss from constant phase shift parameter, optimal phase shift parameter and experimental data.

D. Simulation of the TEAM Problem 32

The proposed inverse vector hysteresis model has been tested by solving TEAM problem 32, which is a benchmark designed to test vector hysteresis models. The testing bench consists of a three-limbed transformer ferromagnetic core made of a pack of five 0.5 mm thick NO electrical steel laminations. The testing case no. 3 is simulated in which the two outer limbs are excited by two sinusoidal voltage sources (10 Hz) with a phase difference of 90° so that significant rotational effects are produced at the T joint. The detailed model dimensions, material properties data and measured data can be found in [31].

The nonlinear relationship of H and B is linearized by means of the fixed-point technique in the following manner:

$$H = v_{FP}B + M(B) \qquad (23)$$

where M is fixed-point residual which is determined by the adopted material model. v_{FP} stands for the fixed-point coefficient which must be constant during iterations for each time step and should be properly chosen to ensure convergence.

By using (23) with magnetic vector potential A, the governing equation, with excitation current J and considering eddy current in a conducting material with conductivity σ, can be expressed as:

$$\nabla \times v_{FP}(\nabla \times A) + \sigma \frac{\partial A}{\partial t} = J - \nabla \times M \qquad (24)$$

For a 2-D system, vector magnetic potential has only z-component and is written as $\sum_{i=1}^{N_t} N_i A_i$. N_t is the total number of nodes, and A_i is the vector potential of node i whose linear shape function is N_i. After applying Galerkin's weighted-residual method over the entire solution region Ω, the following algebraic form of a system of differential equations is obtained:

$$SA + T\frac{dA}{dt} = J + P \qquad (25)$$

with

$$S_{ij} = \int_{\Omega} v_{FP} \nabla N_i \nabla N_j d\Omega \qquad T_{ij} = \int_{\Omega} \sigma N_i N_j d\Omega$$

$$P_i = -\int_{\Omega} (\nabla \times M) N_i d\Omega \qquad J_i = \int_{\Omega} N_i J_m d\Omega \qquad (26)$$

where S is the assembled stiffness matrix and T is a matrix related to the eddy currents in the conducting region. Column vector P is associated with fixed-point residual. J_m is the current density in the coil region.

The local fixed-point coefficient is adopted in order to speed up the iteration. In this case, for each time step k, a local coefficient is computed once for each element according to the magnetic flux density level of the previous time step. During the following iterative calculation of vector magnetic potential, the coefficient and all system matrices remain constant except P, which is adaptively updated at each iteration step n until convergence. By using the implicit Euler scheme for time discretization, the algebraic equation (25) can be written as:

$$(T + \Delta t S_k)A_k^n = TA_{k-1} + \Delta t(J_k + P_k^{n-1}) \qquad (27)$$

where Δt represents the time interval between two time steps. The solving procedure employing fixed-point iteration and the implicit time-stepping scheme is shown in Fig. 15.
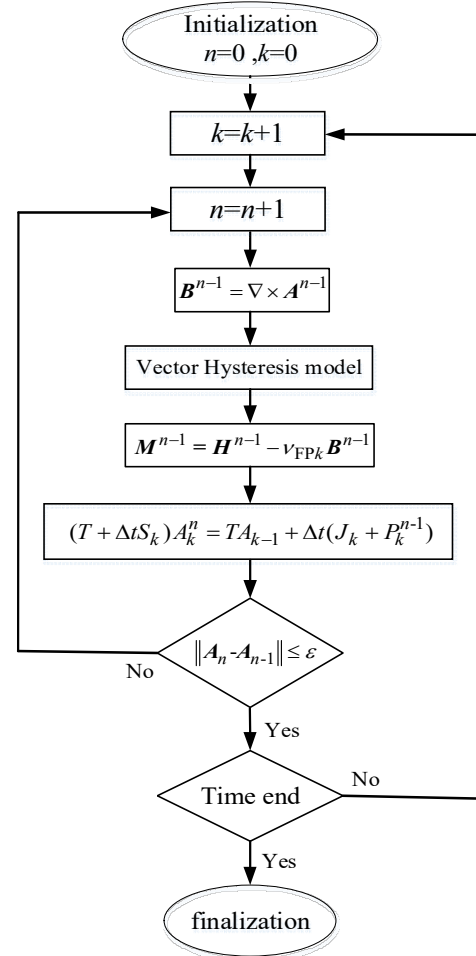
Fig. 15. Flowchart of incorporating inverse vector hysteresis model into 2-D finite element analysis by means of the fixed-point iteration and time-stepping scheme.

The symmetric 2-D mesh has 2886 triangular elements along with 1496 nodes. The number of time steps per period is 500. Note that in the actual calculation, the eddy current in the core region is neglected by setting the conductivity to 0. In order to avoid the problem of many computation cycles being needed if the voltage-driven source is adapted, the measured current waveforms are directly used as the excitation source here. The computed magnetic flux density distribution at time instant (t=0.022 s) is shown in Fig. 16(a). Fig. 16(b) compares the B loci at point P using this inverse vector hysteresis model with the experimental data. It can be seen that the computed curve is in relatively good accordance with the measured data.
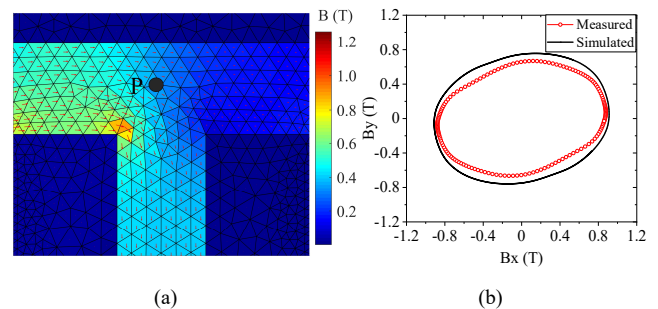
Fig. 16. Simulation results. (a) Magnetic flux density distribution at the T joint at one time instant (t=0.022 s). (b) Measured and computed B loci at point P.

V. CONCLUSION

This paper compares the Mayergoyz-based vector models. A thorough description of the macroscopic anisotropic behavior for NO steel is given and it is demonstrated that the existing vector models usually fail to reproduce the accurate H loci under rotational excitations when H deviates from the RD, especially at low fields. This is because, under this condition, the anisotropy of NO steel is mainly manifested as uniaxial anisotropy along its RD with elliptical loci while these models still generate circular loci.

Based on the above analysis, a modified inverse vector hysteresis model is proposed to describe the anisotropic behavior of NO steel over a wide range of rotational excitations. This model employs a new representation of the vector Everett function and a nonlinear coefficient w in combination to accurately characterize the variation of anisotropy with the excitation level. By comparing with the experimental data, the proposed model is proven to be capable of improving the prediction accuracy of the H loci especially in the TD compared with existing models. However, the core loss estimation is still subject to large errors especially at high inductions. In addition, the TEAM problem 32 (case no. 3) is simulated by coupling this vector model and the solutions also agree well.

REFERENCES

[1] Y. Guo, J. G. Zhu, J. Zhong, H. Lu, and J. X. Jin, "Measurement and modeling of rotational core losses of soft magnetic materials used in electrical machines: A review," *IEEE Transactions on Magnetics,* vol. 44, no. 2, pp. 279-291, Feb. 2008.

[2] J. C. Akiror, A. Merkhouf, C. Hudon, and P. Pillay, "Consideration of design and operation on rotational flux density distributions in hydrogenerator stators," *IEEE Transactions on Energy Conversion,* vol. 30, no. 4, pp. 1585-1594, Dec. 2015.

[3] R. Findlay, N. Stranges, and D. MacKay, "Losses due to rotational flux in three phase induction motors," *IEEE Transactions on Energy Conversion,* vol. 9, no. 3, pp. 543-549, Sep. 1994.

[4] S. E. Zirka, Y. I. Moroz, A. J. Moses, and C. M. Arturi, "Static and dynamic hysteresis models for studying transformer transients," *IEEE Transactions on Power Delivery,* vol. 26, no. 4, pp. 2352-2362, Oct. 2011.

[5] D. C. Jiles, J. Thoelke, and M. Devine, "Numerical determination of hysteresis parameters for the modeling of magnetic properties using the theory of ferromagnetic hysteresis," *IEEE Transactions on Magnetics,* vol. 28, no. 1, pp. 27-35, Jan. 1992.

[6] G. Consolo, G. Finocchio, M. Carpentieri, E. Cardelli, and B. Azzerboni, "About identification of scalar Preisach functions of soft magnetic materials," *IEEE Transactions on Magnetics,* vol. 42, no. 4, pp. 923-926, Apr. 2006.

[7] E. Stoner, and E. Wohlfarth, "A mechanism of magnetic hysteresis in heterogeneous alloys," *IEEE Transactions on Magnetics,* vol. 27, no. 4, pp. 3475-3518, Jul. 1991.

[8] I. D. Mayergoyz, *Mathematical models of hysteresis and their applications*: Academic Press, 2003.

[9] I. Mayergoyz, and A. Adly, "A new isotropic vector Preisach-type model of hysteresis and its identification," *IEEE Transactions on Magnetics,* vol. 29, no. 6, pp. 2377-2379, Nov. 1993.

[10] A. Adly, and I. Mayergoyz, "A new vector Preisach‐type model of hysteresis," *Journal of applied physics,* vol. 73, no. 10, pp. 5824-5826, May. 1993.

[11] E. Dlala, A. Belahcen, K. A. Fonteyn, and M. Belkasim, "Improving loss properties of the Mayergoyz vector hysteresis model," *IEEE Transactions on Magnetics,* vol. 46, no. 3, pp. 918-924, Mar. 2009.

[12] L. Zhu, W. Wu, X. Xu, Y. Guo, W. Li, K. Lu, and C.-S. Koh, "An improved anisotropic vector Preisach hysteresis model taking account of rotating magnetic fields," *IEEE Transactions on Magnetics,* vol. 55, no. 6, Mar. 2019, Art. no. 7300404.

[13] E. Cardelli and A. Faba, "Modelling of vector hysteresis at macromagnetic scale: Open questions and challenges," Physica B: Condensed Matter, vol. 486, pp. 130-137, 2016.

[14] E. Cardelli et al., "A challenging hysteresis operator for the simulation of Goss-textured magnetic materials," Journal of Magnetism and Magnetic Materials, vol. 432, pp. 14-23, 2017.

[15] E. Cardelli, "Advances in Magnetic Hysteresis Modeling," Handbook of Magnetic Materials, pp. 323–409, 2015.

[16] J. Saitz, "Newton-Raphson method and fixed-point technique in finite element computation of magnetic field problems in media with hysteresis," *IEEE Transactions on Magnetics,* vol. 35, no. 3, pp. 1398-1401, May. 1999.

[17] S. E. Zirka, Y. I. Moroz, R. G. Harrison, and N. Chiesa, "Inverse hysteresis models for transient simulation," *IEEE Transactions on Power Delivery,* vol. 29, no. 2, pp. 552-559, Apr. 2014.

[18] S. E. Zirka, Y. I. Moroz, N. Chiesa, R. G. Harrison, and H. K. Høidalen, "Implementation of inverse hysteresis model into EMTP—Part I: Static model," *IEEE Transactions on Power Delivery,* vol. 30, no. 5, pp. 2224-2232, Oct. 2015.

[19] E. Dlala, and A. Arkkio, "Analysis of the convergence of the fixed-point method used for solving nonlinear rotational magnetic field problems," *IEEE transactions on magnetics,* vol. 44, no. 4, pp. 473-478, Apr. 2008.

[20] B. Upadhaya, L. Perkkiö, P. Rasilo, A. Belahcen, P. Handgruber, and A. Arkkio, "Representation of anisotropic magnetic characteristic observed in a non-oriented silicon steel sheet," *AIP Advances,* vol. 10, no. 6, Jun. 2020, Art. no. 065222.

[21] P. Handgruber, A. Stermecki, O. Biro, V. Goričan, E. Dlala, and G. Ofner, "Anisotropic generalization of vector Preisach hysteresis models for nonoriented steels," *IEEE Transactions on Magnetics,* vol. 51, no. 3, Mar. 2015, Art. no. 7300604.

[22] S. Yue, Y. Li, Q. Yang, K. Zhang, and C. Zhang, "Comprehensive investigation of magnetic properties for Fe–Si steel under alternating and rotational magnetizations up to kilohertz range," *IEEE Transactions on Magnetics,* vol. 55, no. 7, Jul. 2019, Art. no. 6100705.

[23] K. Chwastek, "Anisotropic properties of non-oriented steel sheets," *IET Electric Power Applications,* vol. 7, no. 7, pp. 575-579, 2013.

[24] M. Kuczmann, "Vector Preisach hysteresis modeling: Measurement, identification and application," *Physica B: Condensed Matter,* vol. 406, no. 8, pp. 1403-1409, Jan. 2011.

[25] G. Finocchio, M. Carpentieri, E. Cardelli, and B. Azzerboni, "Analytical solution of Everett integral using Lorentzian Preisach function approximation," Journal of magnetism and magnetic materials, vol. 300, no. 2, pp. 451-470, 2006.

[26] Z. Szabó and J. Füzi, "Implementation and identification of Preisach type hysteresis models with Everett Function in closed form," Journal of Magnetism and Magnetic Materials, vol. 406, pp. 251-258, 2016.

[27] S. Naidu, "Simulation of the hysteresis phenomenon using Preisach's theory," *IEE Proceedings A-Physical Science, Measurement and Instrumentation, Management and Education,* vol. 137, no. 2, pp. 73-79, Mar. 1990.

[28] E. Dlala, "Efficient algorithms for the inclusion of the preisach hysteresis model in nonlinear finite-element methods," *IEEE Transactions on Magnetics,* vol. 47, no. 2, pp. 395-408, Feb. 2010.

[29] I. Mayergoyz, and G. Friedman, "On the integral equation of the vector Preisach hysteresis model," *IEEE Transactions on Magnetics,* vol. 23, no. 5, pp. 2638-2640, Sep. 1987.

[30] C. Zhang, Y. Li, J. Li, Q. Yang, and J. Zhu, "Measurement of three-dimensional magnetic properties with feedback control and harmonic compensation," *IEEE Transactions on Industrial Electronics,* vol. 64, no. 3, pp. 2476-2485, Mar. 2017.

[31] O. Bottauscio, M. Chiampi, C. Ragusa, L. Rege, and M. Repetto, "A test case for validation of magnetic field analysis with vector hysteresis," *IEEE Mransactions on Magnetics,* vol. 38, no. 2, pp. 893-896, Mar. 2002.

This article has been accepted for publication in a future issue of this journal, but has not been fully edited. Content may change prior to final publication. Citation information: DOI 10.1109/TEC.2021.3073349, IEEE Transactions on Energy Conversion

> REPLACE THIS LINE WITH YOUR PAPER IDENTIFICATION NUMBER (DOUBLE-CLICK HERE TO EDIT) <   10

Shuaichao Yue was born in Hebei, China, in1992. He received the B.Eng and M.Eng degrees in electrical engineering from Hebei University of Technology, Tianjin, China, in 2012 and 2016. He is currently working towards Ph.D degree in electrical engineering with Hebei University of Technology. He is now a visiting researcher with Wolfson Centre for Magnetics, Cardiff University, Cardiff, UK. His current research interests include measurement of magnetic properties, hysteresis modelling and its application.

Philip I. Anderson was born in U.K., in 1972. He received B.Eng., M.Sc., and Ph.D. degrees from Cardiff University, Cardiff, U.K., in 2000. He was with Cogent Power, Newport, U.K and later, a Researcher at, Cardiff University, where he is currently Reader in Magnetic Engineering.

His current research interests include production, application, and characterissation of soft magnetic materials. Dr. Anderson is a Chartered Engineer and member of national and international standards committees on magnetic steels and alloys. He is currently a member of the international organising committees of several major conference series, including Soft Magnetic Materials.

Yongjian Li was born in Hebei, China, in 1978. He received the B.Eng., M.Eng., and Ph.D. degrees from the Hebei University of Technology (HEBUT), Tianjin, China, in 2002, 2007, and 2011, respectively.

From 2009 to 2011, he was an Assistant Professor in Electromagnetic with the University of Technology Sydney, Ultimo, NSW, Australia. As a Visiting Scholar, he visited Ottawa University, Ottawa, ON, Canada, from 2016 to 2017. In 2002, he joined HEBUT, where he is currently a Professor in Electromagnetic with the School of Electrical Engineering in 2002, and also the Deputy Director of the State Key Laboratory of Reliability and Intelligence of Electrical Equipment. His research interests include measurement of magnetic properties, modeling of magnetic materials, and power electronics.

Qingxin Yang received his B.S., M.S., and Ph.D. degrees from Hebei University of Technology, Tianjin, China, in 1983, 1986, and 1997, respectively. Since 1996, he has been a professor of Hebei University of Technology. From 2008 to 2018, he used to be the president of Tianjin Polytechnic University, China. Since 2018, he has been the president of Tianjin University of Technology, China. He used to be a board member of International COMPUMAG Society and the president of China chapter. Since 2015, he has been the president of China Electrotechnical Society. His research interests include computational electromagnetism, engineering electromagnetism and their applications, special wireless power transfer.

Anthony John Moses was born in Newport, U.K. He received the B.Eng.Tech. degree in electrical engineering, the Ph.D. degree, and the D.Sc. degree for contribution to research into the properties and applications of soft magnetic materials from the University of Wales, Cardiff, U.K., in 1966, 1970, and 1990, respectively, He was appointed as a Professor of Magnetics and the Director of the Wolfson Centre for Magnetics with Cardiff University, Cardiff, in 1992, where he was a Lecturer, Senior Lecturer, and Reader. Since 2012, he has been Emeritus Professor with Cardiff University. His current research interests include properties and applications of magnetic materials. He has authored over 500 publications and supervised over 100 post-graduate students in themes related to the production, characterization, and applications of magnetic materials. Prof. Moses is a fellow of the Institute of Physics and the Institution of Engineering and Technology. He was a Chairman of the U.K. Magnetics Society and the International Organizing Committee of the Soft Magnetic Materials series of conferences. He is a member of organizing and editorial committees of several international conferences and journals.